

# IMMEDIATE ONLINE ACCEPTED (IOA) ARTICLE

This article presented here has been peer reviewed and accepted for publication in CCS Chemistry. The present version of this manuscript has been posted at the request of the author prior to copyediting and composition and will be replaced by the final published version once it is completed. The DOI will remain unchanged.

IOA Posting Date: May 08, 2025

**TITLE:** Identification of Cu-N<sub>2</sub> Sites for Zn-Air Batteries in Harsh Electrolytes: Computer Virtual Screening, Machine Learning, and Practical Application

AUTHORS: Chenxi Xu, Kaiqi Li, Shengchao Liu, Junwei Xu, Subash Sharma, Jincan Zhang, Boyang Mao, Haotian Chen, Hao Zhang, Hannan Xu, Bingcheng Luo, Haiteng Zhao, Zhuoxinran Li, Zhongyuan Huang, Jianan Wang, Kai Xi, Chaopeng Fu, Yunlong Zhao, Guoliang Chai, Guanjie He, Ivan Parkin, Huanxin Li

**DOI:** 10.31635/ccschem.025.202505577

CITE THIS: CCS Chem. 2025, Just Accepted. DOI: 10.31635/ccschem.025.202505577

# Identification of Cu-N<sub>2</sub> Sites for Zn-Air Batteries in Harsh Electrolytes: Computer Virtual Screening, Machine Learning, and Practical Application

Chenxi Xu,<sup>1,14,=</sup> Kaiqi Li,<sup>2,=</sup> Shengchao Liu,<sup>3,=</sup> Junwei Xu,<sup>1</sup> Subash Sharma,<sup>4</sup> Jincan Zhang,<sup>4</sup> Boyang Mao,<sup>4</sup> Haotian Chen,<sup>5</sup> Hao Zhang,<sup>5\*</sup> Hannan Xu,<sup>6</sup> Bingcheng Luo,<sup>7\*</sup> Haiteng Zhao,<sup>8</sup> Zhuoxinran Li,<sup>9</sup> Zhongyuan Huang,<sup>1\*</sup> Jianan Wang,<sup>10</sup> Kai Xi,<sup>10</sup> Chaopeng Fu,<sup>11</sup> Yunlong Zhao,<sup>12</sup> Guoliang Chai,<sup>13</sup> Guanjie He,<sup>2\*</sup> Ivan Parkin,<sup>2\*</sup> Huanxin Li,<sup>2,4,5\*</sup>

- <sup>1</sup> State Key Laboratory for Chemo/Biosensing and Chemometrics, College of Chemistry and Chemical Engineering, Hunan University, Changsha, Hunan, 410082
- <sup>2</sup> University College London, London WC1H 0AJ
- <sup>3</sup> University de Montreal, Montreal, Quebec, H3T 1J4
- <sup>4</sup> Department of Engineering, University of Cambridge, 9 JJ Thomson Avenue, Cambridge, CB3 0FA
- <sup>5</sup> Department of Chemistry, University of Oxford, Oxford OX1 3QZ
- <sup>6</sup> Department of Biochemistry, University of Oxford, Oxford OX1 3QU
- <sup>7</sup> College of Science, China Agricultural University, Beijing, 100083
- <sup>8</sup> School of Intelligence Science and Technology, Peking University, Beijing, 100871
- <sup>9</sup> University of Toronto, Toronto, ON M5S 1A1
- <sup>10</sup> Department of Environmental Science and Engineering, School of Energy and Power

Engineering, Xi'an Jiaotong University, 28 Xianning West Road, Xi'an 710049

- <sup>11</sup> School of Materials Science and Engineering, Shanghai Jiao Tong University, Shanghai, 20024
- <sup>12</sup> Dyson School of Design Engineering, Imperial College London, London SW7 2BX
- <sup>13</sup> State Key Laboratory of Structural Chemistry, Fujian Institute of Research on the Structure of Matter, Chinese Academy of Sciences (CAS), Fuzhou, Fujian, 350002
- <sup>14</sup> School of Chemistry and Chemical Engineering, Central South University of Forestry and Technology, Changsha, Hunan, 410004
- <sup>=</sup> These authors contributed equally

#### Abstract:

Non-precious-metal catalysts possess great potential to replace noble metals in catalysis; however, selecting efficient candidates through experiments is timeconsuming and costly. Herein, we employ a data-driven virtual screening (VS) method to discover new electrocatalysts. Specifically, we identify Cu-N<sub>2</sub> sites for Zn-air batteries in harsh electrolytes combining VS and machine learning (ML) techniques. A thermodynamically stable and highly active Cu-N<sub>2</sub> Lewis acid site was pinpointed using molecular dynamics (MD) simulations and density functional theory (DFT) calculations. MD simulations filtered stable structures, while DFT calculations exclude those with high overpotentials by evaluating adsorption energies of oxygen-intermediates using "Volcano plots" theory. The ML model, trained in atomic types and geometries, predicts catalysts with DFT-level accuracy. The as-predicted Cu-N<sub>2</sub> Lewis acid site was experimentally synthesized in a hollow nitrogen-doped octahedron carbon framework (Cu-N<sub>2</sub>@HNOC), with a high Cu loading of 13.1 wt%. A Zn-air battery with Cu-N<sub>2</sub>@HNOC as the cathode catalyst showed prolonged cycling stability and high maximum power density of 78.1 mW/cm<sup>2</sup>. Our strategy is applicable to seek valuable catalysts across a wide range of applications. With the accumulation and experimental validation of datasets to improve quality, it is expected to accurately predict promising electrocatalysts by integrating deep ML.

**Keywords:** computer virtual screening, molecular dynamics simulation, DFT calculation, Cu-N<sub>2</sub>-C, Zn-air batteries

#### 1. Introduction

The hysteresis of oxygen reduction reaction (ORR) kinetics restricts the overall development of advanced electrochemical conversion and storage devices, such as metal-air batteries and fuel cells.<sup>[1-4]</sup> It is highly desirable but challenging to accelerate the reaction rate of ORR process by introducing suitable catalysts.<sup>[5-7]</sup> Currently, Pt and its alloys are recognized as state-of-the-art ORR catalysts due to their high activity, but these kinds of catalysts always suffer from poor methanol tolerance, high cost and chemical susceptibility. Therefore, the exploration of non-precious metal-based ORR catalysts with low cost, high activity and good durability is highly desired. <sup>[8-10]</sup>

M-N-C (M=Fe, Co, Ni, Cu etc.) catalysts are emerging non-precious metal-based electrocatalysts.[11-13] Among them, Cu-based catalysts are regarded as promising alternatives to replace Pt owing to their acceptable price, potential ORR activity and superior electrical conductivity [14] Despite the intrinsic activity of Cu being lower than most of non-precious metals (including Ca, Mg, Al, Zn, Fe, Co, Ni, Sn, Pb etc.), Cu-N<sub>x</sub> sites were demonstrated to deliver efficient activity towards oxygen catalytic process because the N ligands will significantly modulate the electronic structure of Cu thus optimizing adsorption energies towards oxygen intermediates.[15-17] Yang et al. found that Cu-N<sub>x</sub> structures can adjust the density of states of carbon near the Fermi level, and lower the local work function, thus promoting activity towards ORR<sup>[18]</sup>. For Fe-N-C sites with strong O\* adsorption, the intermediates adsorption energy will be reduced by increasing coordination number to promote the activity, proved by Lai et al.[19] Their results revealed that the oversaturated Fe-N<sub>5</sub> active sites showed better activity than Fe-N<sub>4</sub>. DFT calculations attested that unsaturated Cu-N<sub>x</sub>-C sites (e.g. Cu-N<sub>2</sub>, Cu-N<sub>3</sub> sites) possess more suitable binding energy toward oxygen intermediates than the saturated Cu–N<sub>4</sub>-C site, thus delivering higher ORR activity.<sup>[20-22]</sup>

However, several challenges hindered the exploration of Cu-N<sub>x</sub>-C sites with efficient electrochemical activities. First, the search for thermodynamic stable Cu-N<sub>x</sub>-C sites based on experimental results is an extremely time-consuming and capital-sensitive task. Furthermore, the fabrication of thermodynamic stable and highly active Cu-N<sub>x</sub>-C sites is still challenging, especially at high loading of single Cu atoms (>10.0 wt.%). Therefore, it is not feasible to screen such catalysts based on an "inch-by-inch "search mode *via* typical experimental synthesis, characterization, and electrochemical measurement. Computer virtual screening (VS) technology is an efficient approach to accelerate the conventional high throughput screening (HTS) processes that have been successfully applied for new drug discovery in the pharmaceutical industry recently. The computer VS approach is expected to be applicable to search for suitable catalysts in broad areas, although no standard protocol has been established yet and no case to our knowledge reported up to now.

Herein, considering the above challenges, we firstly use the computer VS mode to discover new efficient electrochemical catalysts, which are more cost-effective than experimental ones. First, we employed molecular dynamics (MD) simulation to discover coordination unsaturate Cu-N<sub>2</sub> Lewis acid sites that are thermodynamically stable (for easy synthesis purpose) and harsh electrolytes (1M KOH and 0.5 M H<sub>2</sub>SO<sub>4</sub>, for wide pH applications). Then, DFT calculations were adopted to filter out those sites with high overpotential by evaluating the adsorption energies for oxygen-related adsorption intermediates based on "Volcano plots" theory and effective description factor. The as-predicted thermodynamic stable yet coordination unsaturated Cu-N<sub>2</sub> sites was further synthesized *via* a facile *in-situ* self-template induced strategy in a hollow nitrogen-doped octahedron carbon (Cu-N<sub>2</sub>@HNOC), in which Cu atoms are coordinated with two N atoms (Cu-N<sub>2</sub>) in linear mode on the planar defects, confirmed by quantitative XAS analysis, Raman fitting, XPS and theoretical simulations. The

synthesis of Cu-N<sub>2</sub>@HNOC with valence state of Cu close to +1 within a linear type of Cu-N<sub>2</sub> site is quite challenging but we successfully achieved this using a straightforward *in-situ* self-template strategy, as outlined in the **Supplementary Information (SI)**, which builds upon our previous experiments. As a result, both experimental data and DFT calculations verified that the Cu-N<sub>2</sub> Lewis acid sites exhibit both promising electrochemical activity ( $E_{onset}$  = 0.93 V,  $E_{1/2}$  = 0.83 V and  $J_{L}$  = 5.81 mA/cm<sup>2</sup>) and long-term stability for ORR over a wide pH range. The as-prepared Cu-N<sub>2</sub>@HNOC was also fabricated as cathode catalysts in Zn-air batteries, delivering a peak power density of 190 mW/cm<sup>2</sup> at a current density of 312 mA/cm<sup>2</sup>. Notably, the Cu-N<sub>2</sub>-C site also exhibits the highest stability compared to the other representative non-precious metals (Fe, Co, Ni etc.) due to the low intrinsic activity of Cu element, and thus a stable cycling at acid electrolyte was achieved, outperforming the state-of-the-art Zn-air batteries.

## 2. Experimental Methods

Chemicals and materials: Copper nitrate trihydrate, zinc acetate, sodium hydroxide (NaOH), polypyrrole hydrazine hydrate (85%), hydrochloric acid (HCl, 36.0~38.0%), potassium hydroxide (KOH) and ethanol were analytical reagent-grade (AR) and purchased from Sinopharm Chemical Reagent Co. Ltd. (Shanghai, China). Zinc foil (99.9% trace metals basis), polyvinyl alcohol, commercial Pt/C (20 wt %) and RuO2 catalysts were supplied by Sigma-Aldrich. All chemicals were used without further purification.

Syntheses of CuO octahedron: 0.6 g of copper ( II ) nitrate trihydrate was dissolved in 1 L of deionized water under continuous stirring for 30 minutes. Subsequently, 10 mL of 2 M NaOH aqueous solution and 2 mL 35% hydrazine hydrate were sequentially added under stirring condition for 2 hours. After centrifugation and drying at 60°C

overnight, the obtained powder was calcinated in air at 400 °C for 30 minutes with a heating rate of 2°C/min to acquire the black product, which was denoted as CuO octahedron.

Syntheses of Cu-N<sub>2</sub>@HNOC: Firstly, 0.1 g of CuO octahedron and 1 mL of pyrrole were uniformly dispersed in 50 mL of ethanol by ultrasonication for half an hour. Then, 10 mL of 1 M HCl aqueous solution was added dropwise into the above suspension, and kept stirred continuously for 3 h. After centrifugation and washing by deionized water and ethanol, the black product, Cu-containing hollow polypyrrole octahedron (named as Cu-PPY-HO) could be obtained. Finally, the attained Cu-PPY-HO was pyrolyzed at  $800^{\circ}$ C for 2 h in N<sub>2</sub> atmosphere with a heating rate of  $5^{\circ}$ C/min to obtain Cu-N<sub>2</sub>@HNOC. For comparison, hollow nitrogen-doped octahedron carbon (HNOC) was also prepared by washing Cu-PPY-HO in 1 M HCl aqueous solution and deionized water several times, followed by the same pyrolysis procedure of Cu-N<sub>2</sub>@HNOC.

#### 3. Results and Discussion

Technically, We propose an advanced multi-modal model to demonstrate the effectiveness of virtual screening (VS) for electrocatalysts. This model integrates geometric deep learning, quantum chemistry, and the XGBoost (eXtreme Gradient Boosting) machine learning algorithm for predicting the ORR overpotential profile. The predictions are then validated experimentally. Geometric deep learning is employed to identify element types and atomic positions within chemical structures. (Scheme 1a). Quantum chemistry provides fundamental physical and chemical properties regarding the ORR, as well as the electrocatalytic performance indicators for these structures (Figure S1), while XGBoost guides subsequent alterations to the chemical structure (Scheme 1b). The optimized chemical structure is synthesized and tested for experimental validation, with relevant data weighting adjusted based on reliability

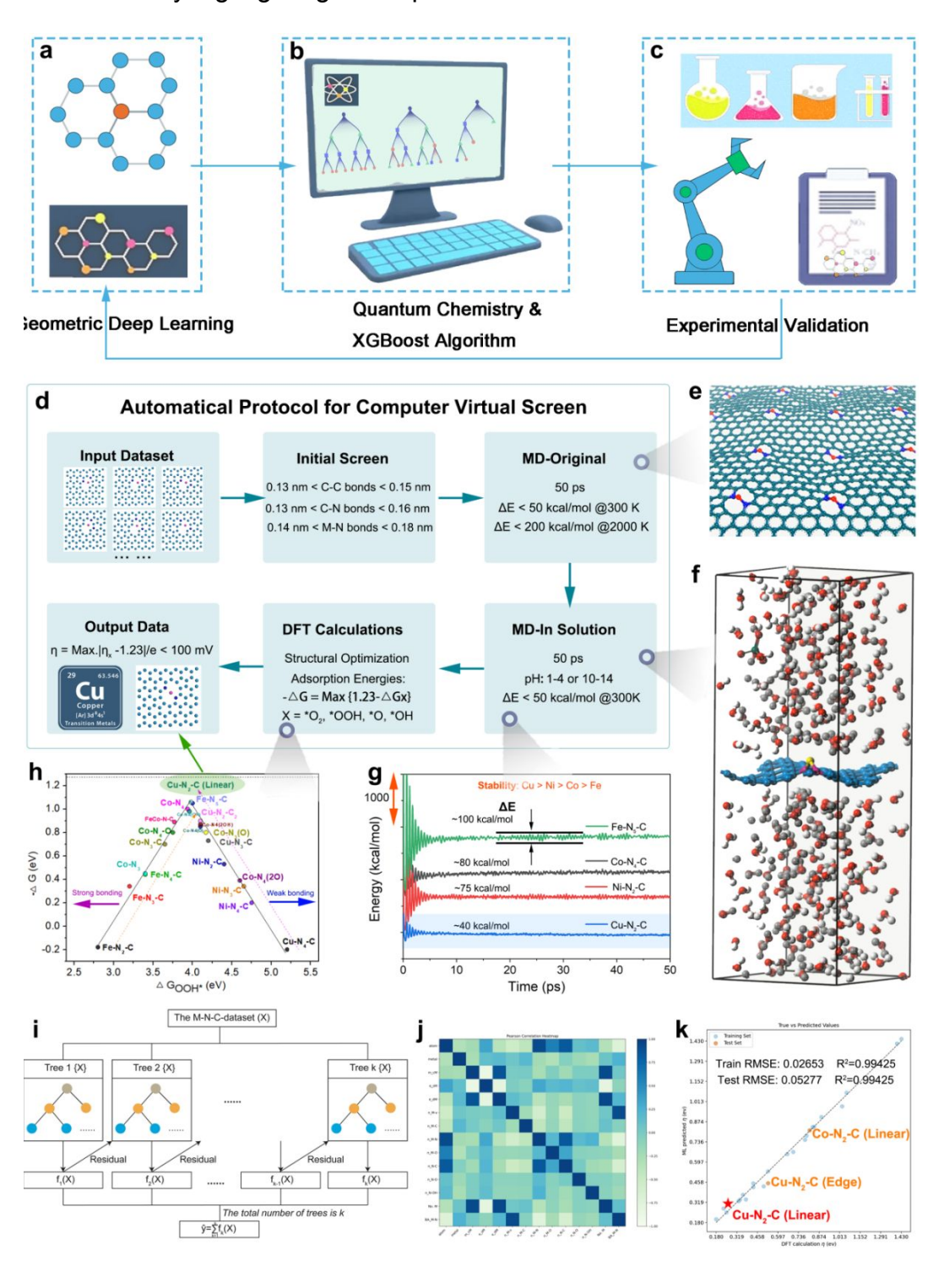
feedback from experimental outcomes (Scheme 1c). Specifically, our observations indicate that virtual screening (VS) effectively retrieves catalyst-activity-stability relations and accurately predicts electrocatalyst structures to achieve desired properties. These functionalities hold promise for accelerating various catalyst discovery processes. Furthermore, the outcomes of such catalyst structures consistently align with feedback from chemical synthesis experiments, showcasing the model's adeptness in domain knowledge exploration. Scheme 1d shows the standard protocol for searching efficient M-N<sub>x</sub>-C (M=Fe, Co, Ni and Cu; x=2, 3, 4, and 5) active sites. The input dataset were randomly generated by slightly modifying the graphene structure model (replacing carbon atoms with defects, N atoms, or Cu atoms, details in Supporting Information). Then, an initial screening was conducted to check whether the bond lengths of C-C, C-N and M-N are within a rational range. The next step was to run an MD simulation to confirm the stability of input rational structures at both room temperature and high temperature, with restrictive conditions on energy fluctuations setting as  $\Delta E$  < 0.5 kcal/mol @300 K; and  $\Delta E$  < 5.0 kcal/mol @2000 K within 50 ps to ensure good thermal stability, which is essential for easy and scalable synthesis. The representative structural model is shown in **Scheme 1e**. Meanwhile, the structural dynamic stability was also verified in harsh electrolyte conditions with  $\Delta E$  < 0.5 kcal/mol @300 K to check the long-term durability in extreme strong acidic or alkaline electrolytes, which is the normal condition in electrocatalytic systems. Scheme 1f displays the selected structural model in an extreme acidic solution (0.5 M H<sub>2</sub>SO<sub>4</sub>), and **Scheme 1g** illustrated the energy profiles after 50 ps, indicating the good stability. Moreover, the dynamic stable structures were carried out with DFT calculations to quantify the theoretical overpotential by evaluating their adsorption energies for oxygen-related adsorption intermediates, e.g. \*O<sub>2</sub>, \*OOH, \*O, and \*OH (**Scheme 1h**), and the potential candidate was selected based on the "Volcano plots" theory.

Normally, the changes in Gibbs free energy for adsorbed oxygen-related intermediate  $(\triangle G_{^*OOH})$  will increase with coordination number of N (M-N<sub>5</sub>-C > M-N<sub>4</sub>-C > M-N<sub>3</sub>-C > M-N<sub>2</sub>-C), indicating the adsorption ability alters from strong to weak. The Fe-N<sub>x</sub>-C sites have a relatively strong adsorption ability towards intermediates, and the catalytic activity could be improved by increasing the coordination number of N. Thus, the Fe-N<sub>5</sub>-C is on the top of the "Volcano plots", suggesting the highest catalytic activity. The opposite trend was seen for Ni-N-C catalysts which displayed a catalytic activity order of Ni-N<sub>4</sub>-C > Ni-N<sub>3</sub>-C > Ni-N<sub>2</sub>-C due to the weak adsorption on Ni sites. Following this rule, the catalytic activity of Cu-N<sub>2</sub>-C sites should exceed the Cu-N<sub>4</sub>-C and Cu-N<sub>3</sub>-C sties, and we predict its location at the top of the "Volcano plots" according to the Gibbs free energy for \*OOH. Finally, the stability of representative high-active structure models Fe-N<sub>5</sub>-C, Co-N<sub>4</sub>-C, Ni-N<sub>2</sub>-C and Cu-N<sub>2</sub>-C were conducted with MD simulations in acid solution, resulting in energy vibrations of ~100, 80, 75, and 40 kcal/mol, which indicates the Cu-N<sub>2</sub>-C is the most stable structure due to the intrinsic inertness of Cu among all the high-active structure models. Only the structures with the limited energy vibration (<50 kcal/mol) for MD simulation were collected in the output data. As a result, the Cu-N<sub>2</sub> Lewis acid site in linear mode was predicted as a model with thermodynamic stability and high catalytic activity simultaneously.

With the accumulation of overpotential profiles from DFT calculations, it becomes feasible to use machine learning algorithms to predict catalysts based on the M-N-C dataset, which significantly accelerates the screening and prediction process. The M-N-C dataset is trained and evaluated with XGBoost (**Scheme 1i**), an algorithm designed to construct Decision Trees (DTs). XGBoost classifies the M-N-C dataset by continuously building DTs and learning from misclassifications or residues. Eventually, all the DTs are combined to assist with predictions. DTs are similar to human thinking in their intelligible nature, making XGBoost an extremely competitive machine learning

Firstly, we collected and listed 25 selected M-N-C models as dataset model.<sup>[23]</sup> (Figure S1). We adopt XGBoost, a machine learning algorithm that combines prediction results of multiple tree models to achieve better generalization performance, for predicting the overpotential voltage for ORR. We take 14 descriptors which are able to be obtained directly from the M-N-C model dataset: CN atom (coordination number of center metal), metal (type of center metal), m cM (mass of center metal), e sM (Number of electrons in the s orbital for center metal), e dM (Number of electrons in the d orbital for center metal), n M-v (number of vacant coordination for center metal), n M-C (number of carbon coordination for the center metal), n M-N (number of nitrogen coordination for the center metal), n M-O (number of oxygen coordination for the center metal), n\_N-C (number of nitrogen-carbon bonds), n\_N-O (number of nitrogen-oxygen bonds), n N-OH (number of N-OH bonds), No. M (Metal atomic number), BA M-N (bond angle of Metal-Nitrogen). We calculated the Pearson correlation among these 14 descriptors, with the heatmap shown in **Scheme 1**j. These 14 descriptors were then fed into the XGBoost model to predict the overpotential profile. The training objective was to minimize the root mean squared error (RMSE) between the ground-truth overpotential profile and the predicted overpotential profile. We employed grid search to select the optimal hyperparameters, including learning rate, maximum tree depth, feature subsample ratio, and the number of trees. The optimal hyperparameters are listed in the SI, and the prediction results are illustrated in **Scheme 1k**. The training RMSE is 0.02653 and the test RMSE is 0.05277, indicating that the predicted data aligns well with the DFT data. The Cu-N<sub>2</sub>-C (linear) model is identified as the predicted electrocatalytic site for ORR with low overpotential (denoted by the red star in **Scheme 1k**). We further demonstrate feature importance in **Figure S2**, where the CN atom plays the most significant role (17.8%), followed by metal (15.8%), m cM (11.6%), n M-N (11.0%), n M-C (8.9%), and BA M-N (7.5%). The

other features are less important, each with an importance of less than 7%. In summary, this machine learning algorithm enables accurate evaluation and prediction of electrocatalyst performance based on the atomic types and geometric model of M-N-C profiles. Additionally, it provides insights into the design principles and optimization basis for M-N-C by highlighting the importance of various features.



Scheme 1. Schematic representation of processes for computer virtual screen: (a) geometric deep learning, (b) gaussian processes and bayesian optimization, (c) experimental validation, (d) the standard protocol, (e) MD screened thermodynamic stable structure from 300 to 2000 K, and (f) stability in harsh electrolyte (pH: 1-4 or 10-14), (g) energy profiles during MD and (h) band structures and adsorption energies of intermediates from DFT calculations, (i) XGBoost algorithm for mechine learning, (j) Pearson correlation coeeficient heatmap among 14 descriptors, (k) Comparison of DFT-calculated overpotential profiles with ML-predicted ones.

To demonstrate the catalytic activity and thermodynamic stability of the Cu-N<sub>2</sub> Lewis acid site in linear mode for ORR, detailed MD and DFT simulations in the VS protocol were illustrated. The model of Cu-N<sub>2</sub>-C sites was built up by replacing two carbon atoms in opposite positions with nitrogen atoms and removing adjacent carbon atoms to create defects for the two coordinated copper atom. The adsorption behavior for \*O<sub>2</sub>, \*OOH, \*O and \*OH intermediates on Cu-N<sub>2</sub>-C sites are illustrated in **Figure** 1a, suggesting that the Cu center is the active site for ORR. The band structure of the as-constructed Cu-N<sub>2</sub>-C is shown in **Figure 1b**, indicating an enrichment of density of states (DOS) near the Fermi level compare to ideal graphene (zero at Fermi level). The increase in DOS observed in Cu-N<sub>2</sub>-C compared to ideal graphene directly correlates with an enhanced ability to adsorb and activate oxygen intermediates, thereby improving its catalytic efficiency. The electronic structure tuning via Cu-N coordination represents a promising strategy for designing advanced carbon-based catalysts. The model for Cu-N<sub>2</sub>-C exhibits moderate free energies for intermediate adsorption and removal, making the energy barriers more average for all steps. The band structure for Cu-N<sub>2</sub>-C (**Figure 1c**) demonstrates a relatively high density of state as the electron cloud appears near the Fermi level, indicating an enhanced conductivity compared to conventional graphitized carbon materials. The free energies of intermediates on Cu-N<sub>2</sub>-C model for ORR processes at different voltages are shown in Figure 1d, indicating that the step from \*O<sub>2</sub> to \*OOH is the rate determining step (RDS) at 1.23 V. The energy barriers for each step revealed a low overpotential of 0.29 V for the whole ORR process. Therefore, the low energy barrier was achieved for Cu-N<sub>2</sub>-C due to the modulated band structures and DOS, which promoted the kinetics for ORR catalytic processes. Moreover, the thermodynamic stability is as important as catalytic activity for the practical applications. Thus, the MD simulation (Figure 1e) was carried out to investigate the possible degradation of Cu-N2-C under high temperature (2,000K). The simulation results show that Cu-N<sub>2</sub>-C skeleton structure will become wavy but remain undamaged, and all Cu single atoms are well-fixed by N atoms without any aggregation. The MD simulation suggests the as-prepared Cu-N<sub>2</sub>@HNOC catalyst possesses a coordination unsaturated but thermodynamic stable structure, endowing possibly good cyclability of the catalyst. The corresponding HRTEM mapping images (Figure S3, S4) and XPS spectra (Figure S5) of Cu-N<sub>2</sub>@HNOC catalyst after 2000K heat-treatment indicate the Cu single atom persists (the boiling point of copper is above 2900K) and the Cu-N bonds and structures remain unchanged, which verified the good stability of the Cu-N<sub>2</sub> Lewis acid structure under high temperature. In addition, the Cu-N<sub>2</sub>-C in 0.5 M H<sub>2</sub>SO<sub>4</sub> solution was also simulated by MD (Figure 1f, Figure S6 and Videos in Supporting Information) to understand the possible degradation behaviors of Cu-N<sub>2</sub>@HNOC in aqueous acidic electrolytes. The results reveal that: (1) The Cu-N<sub>2</sub>-C skeleton structure becomes wavy and the molecule (H<sub>2</sub>O) and ions (H<sub>3</sub>O<sup>+</sup>, OH<sup>-</sup>) in aqueous electrolytes tend to approach the surface of Cu-N2-C layer, indicating the good hydrophilicity and wettability; (2) The aqueous acidic electrolyte will not etch the Cu-N<sub>2</sub>-C skeleton structure due to the strong coordination bond between the Cu and N atoms, ensuring the excellent catalytic activity and stability of the unsaturated Cu-N<sub>2</sub> Lewis acid sites. It is worth mentioning that the cost for discovering a new catalyst *via* 

VS is much lower than that through experimental approaches. We estimated and compared the cost, time, and energy consumption for evaluating the activity and stability of an individual catalyst via experimental or computer VS approach, and suggest that the VS would be a more cost-, time-, and energy-efficient way of reducing the cost, time, and energy consumption by 80%, 90% and 60%, respectively (Figure S7 and Table S1-S3).

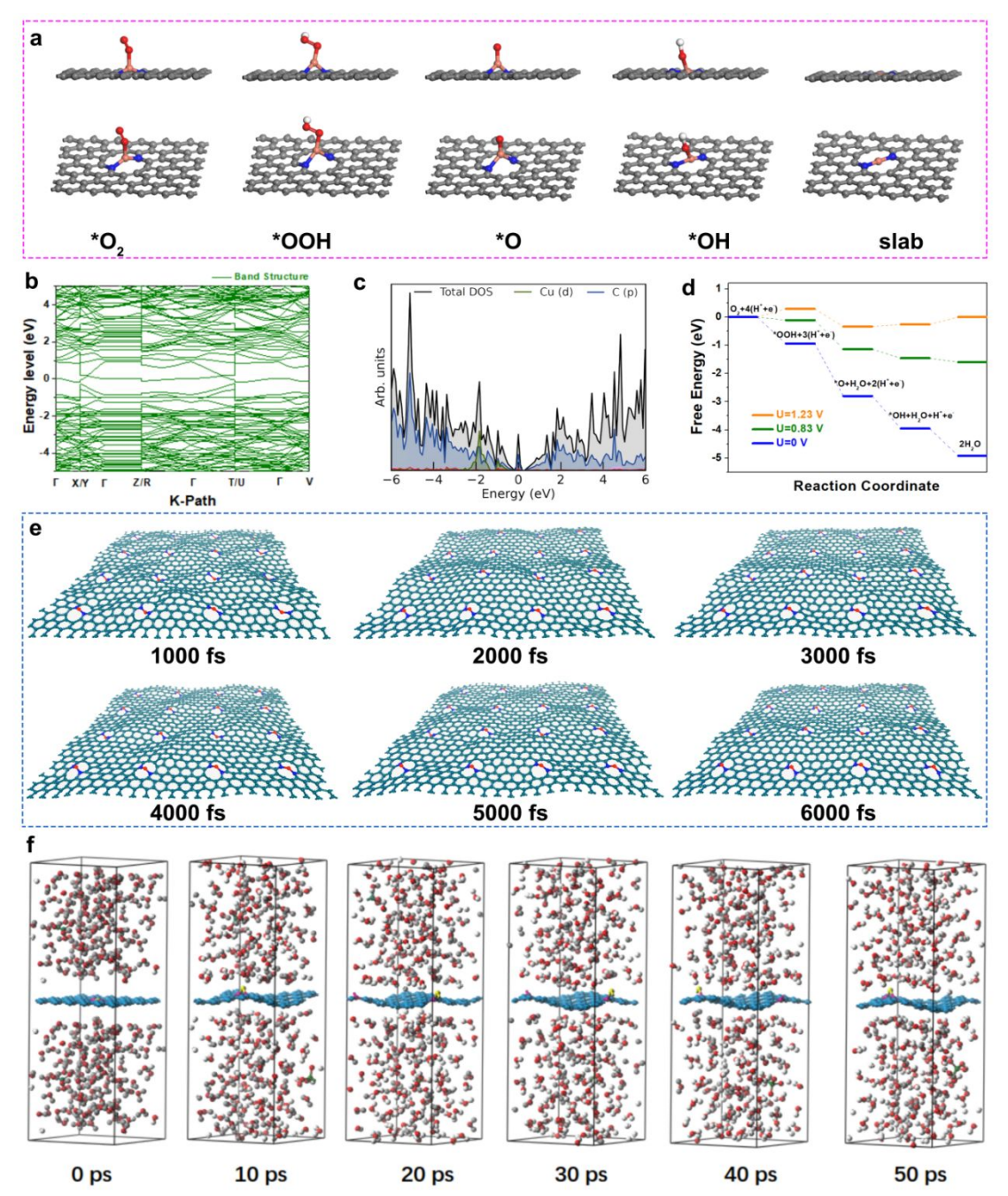


**Figure 1.** (a) Top (up) and side (down) views of the optimized configuration of oxygen intermediate species adsorbed on the  $Cu-N_2-C$ ; (b) The band structure for  $Cu-N_2-C$ ; 13

(c) ORR free energy diagrams at different potentials for Cu-N<sub>2</sub>-C; (d) Gibbs free energy changes for oxygen-containing intermediates on Cu-N<sub>2</sub>-C; (e) the molecular dynamic (MD) simulation at 2,000 K and (f) in 0.5 M H<sub>2</sub>SO<sub>4</sub> solution for Cu-N<sub>2</sub>-C model.

To further verify the accuracy of the algorithm and VS protocol, the as-predicted Cu-N<sub>2</sub> Lewis acid site was experimentally synthesized in a hollow nitrogen-doped octahedron carbon framework (Cu-N<sub>2</sub>@HNOC), in which an ultra-high loading of single Cu atoms (13.1 wt% by ICP-MS) was achieved. As presented in Figure 2a, Cu- $N_2$ @HNOC was fabricated by *in-situ* polymerization followed by the pyrolysis process. Firstly, CuO octahedron with an average diameter of 500 nm (Figure 2b) were prepared by a simple chemical reduction method. The XRD pattern (Figure S8a) and Raman spectrum (Figure S8b) were indexed to the typical characteristic peaks of CuO. Then the CuO template was mixed with pyrrole monomers under ultrasonication. Subsequently, with the addition of diluted hydrochloric acid solution, Cu<sup>2+</sup> ions were gradually released, which initiated the polymerization of pyrrole under the surface of octahedron template until CuO was entirely dissolved. Meanwhile, Cu2+ ions as the oxidant were reduced to low valence states, and trapped by the nitrogen-containing groups of the polymers. The obtained Cu-containing hollow polypyrrole octahedron (Cu-ppy-HO) exhibits the original octahedron shapes (Figure 2c), but its diameter is slightly larger than that of pristine CuO octahedron due to the successful deposition of polypyrrole. The XRD result (Figure S8a) also demonstrated the existence of polypyrrole and the disappearance of CuO after in-situ polymerization. Finally, the Cuppy-HO was annealed in N<sub>2</sub> atmosphere to obtain the final product of Cu-N<sub>2</sub>@HNOC. As depicted in Figure 2d, Cu-N<sub>2</sub>@HNOC presents identical octahedron structures with rough surfaces and hollow structures (in the red circle). The TEM image (Figure 2e) also verified its hollow octahedron structure with the inner and outer diameters of 500 and 700 nm respectively, suggesting the thickness of the carbon shell layer is around

100 nm. The high-resolution TEM image (**Figure 2f**) showed typical amorphous carbon structure without any metal fingerprint, which corresponds to the XRD results (**Figure S8a**). It indicates that there are no peaks of metallic Cu or other compounds in Cu-N<sub>2</sub>@HNOC. Furthermore, only some concentrated bright particles can be observed in the AC HADDF-STEM image (**Figure 2g**), suggesting the existence of atomic-scale Cu sites. The abundant and uniformly-dispersed Cu atoms identified by the isolated bright dots can act as efficient active sites for superior catalytic ability. Moreover, the typical EDS mapping images of Cu-N<sub>2</sub>@HNOC (**Figure 2h**) also disclose that high-loading nitrogen and copper atoms can be distributed evenly on the carbon matrix by this *in-situ* polymerization strategy. Inductively coupled plasma mass spectrometry (ICP-MS) confirmed that the Cu content of 13.1 wt% in Cu-N<sub>2</sub>@HNOC, which is basically consistent with the result of Thermo gravimetric analysis (TGA, in **Figure S9**).

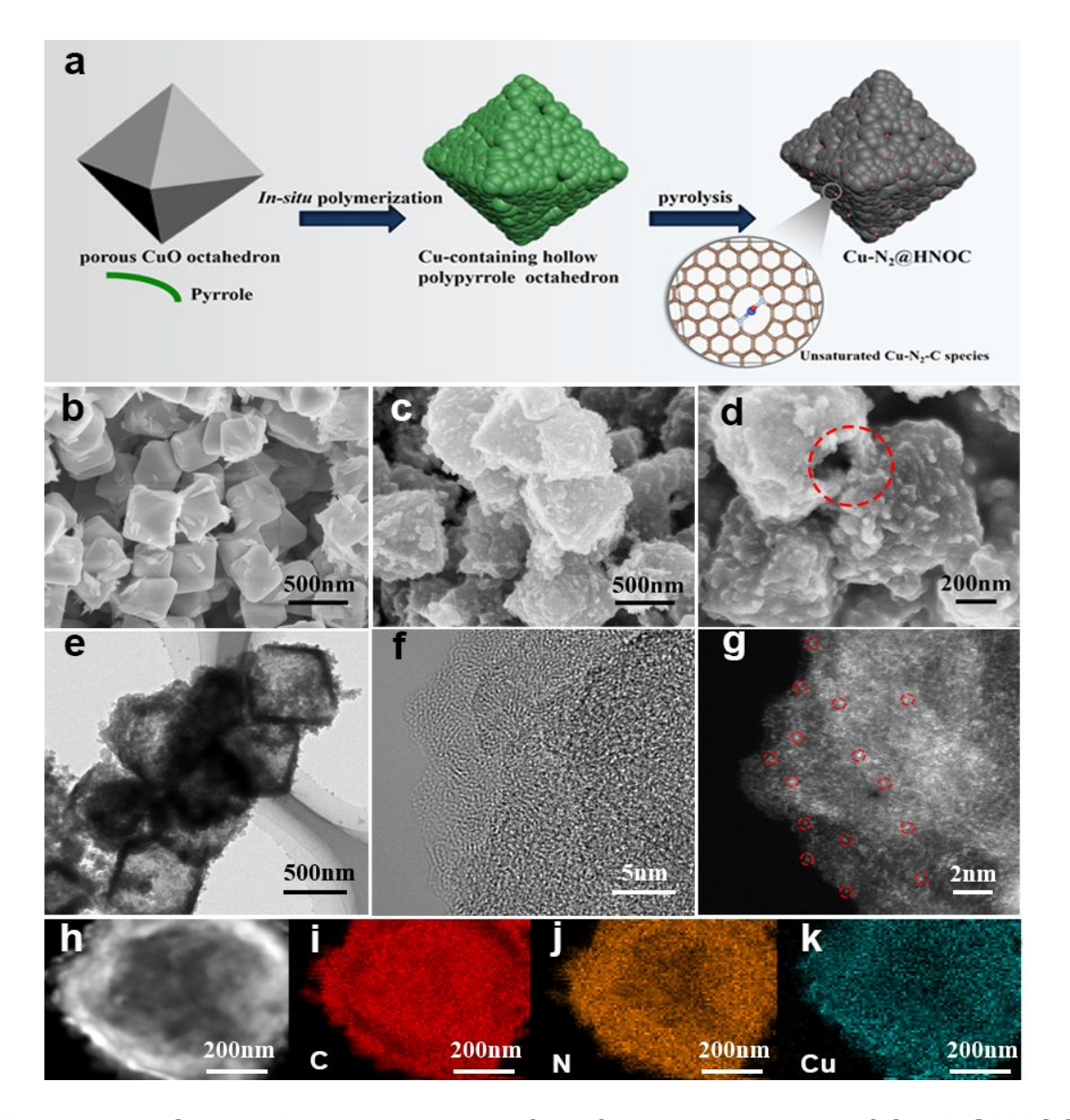


**Figure 2.** (a) Schematic representation of the fabrication process of  $Cu-N_2@HNOC$ ; SEM images of (b) CuO, (c) Cu-ppy HCO, (d)  $Cu-N_2@HNOC$ ; (e) TEM image, (f) HR-TEM image, (g) aberration-corrected HAADF-STEM images and (h-k) corresponding EDS mapping images of  $Cu-N_2@HNOC$ .

X-ray photoelectron spectroscopy (XPS) measurements were carried out to explore the state of each chemical composition. The survey spectrum (**Figure S10**) shows that  $Cu-N_2@HNOC$  contains C, N, O, Cu elements. In the N 1s fine spectrum (**Figure S11a** and **Table S4**), the peaks can be assigned to pyridinic-N, Cu-N, pyrrolic-N and graphitic-N. The peak at 399.1 eV matches Cu-N structure and its content exceeds a quarter, suggesting the abundant Cu-N bonds in Cu-N<sub>2</sub>@HNOC.<sup>[22]</sup> The

high-resolution Cu 2p spectrum (Figure S11b) can be deconvoluted into two peaks at 931.6 and 951.6 eV, which are assigned to Cu(I)  $2p_{1/2}$  and Cu(I)  $2p_{3/2}$  respectively. [22] The results are consistent with the previous reports, that the valence of Cu in unsaturated Cu-N<sub>x</sub>-C sites approaches to +1, while the valence of Cu in saturated Cu-N<sub>4</sub>-C is close to +2.[24,25] The coordination environment and chemical state of Cu atoms were further analyzed by X-ray absorption spectroscopy (XAS) analysis. Figure 3a shows the normalized X-ray adsorption near edge structure (XANES) curve of the Cu k-edge. The adsorption edge of Cu-N2@HNOC is located between that of Cu foil and Cu phthalocyanine (CuPc), suggesting that the oxidization state of Cu species in Cu-N<sub>2</sub>@HNOC was between 0 to 2 (higher than Cu<sup>0</sup> and lower than Cu<sup>2+</sup>). The kspace EXAFS spectra of Cu foil, CuO, Cu<sub>2</sub>O, CuPc and Cu–N<sub>2</sub>@HNOC are illustrated in **Figure S12**. The coordination environment of Cu was fitted by the  $k^3$ -weighted Fourier transforms (FT) of extended X-ray adsorption fine structure (EXAFS, Figure 3b). The result for Cu-N<sub>2</sub>@HNOC showed the existence of a main peak at 1.5 Å which is attributed to Cu-N scattering path according to the referred characteristic peak of Cu-N bond in CuPc. The metallic Cu-Cu peaks at around 2.2 Å in Cu-N₂@HNOC are negligible, indicating the Cu atoms are isolated from each other. The FT-EXAFS fitting results quantified the atomic-coordination numbers of the central Cu atom with N atoms in the first coordination shell, where the  $k^3$ -weighted FT-EXAFS curves were well-fitted with the linear Cu- $N_2$  model in both R space (**Figure 3c**) and k space (**Figure 3d**). The detailed fitting for Cu-N<sub>2</sub>@HNOC with angled Cu-N<sub>2</sub>-C, linear Cu-N<sub>2</sub>-C, Cu-N<sub>3</sub>-C and Cu-N<sub>4</sub>-C models are shown in **Figure S13**, indicating the linear Cu-N<sub>2</sub> model was the best-matched structural fitting. Furthermore, wavelet transform (WT) plot was depicted in Figure 3e and Figure S14. The intensity maximum of Cu foil was centered on around 8 Å, corresponding to the Cu-Cu bonding. In contrast, the maximum of Cu-N<sub>2</sub>@HNOC appeared at 4-6 Å, close to that of CoPc, assigning to the contribution of Cu-N bonding. More detailed structural parameters were listed in **Table S5**. The coordination number of Cu-N<sub>2</sub>@HNOC is  $2.11\pm0.24$  as confirmed by XAS. Compared with Cu-N<sub>4</sub> sites, unsaturated Cu-N<sub>2</sub> are more favorable for O<sub>2</sub> adsorption and O-O bond stretching, so Cu-N<sub>2</sub>@HNOC is expected to deliver an impressive ORR performance. Raman spectroscopy was used to identify the structure of the Cu-N<sub>2</sub> sites in Cu-N<sub>2</sub>@HNOC. **Figure 3g** is the Raman selected area mapping and a typical spectrum for Cu-N<sub>2</sub>@HNOC, which demonstrate the characteristic D peak (~1350 cm<sup>-1</sup>) and G peak (~1580 cm<sup>-1</sup>) for graphite carbon<sup>[26]</sup>. **Figure 3h** illustrated the 143 single-point Raman spectra within the mapping area, where the Raman signals showed slight shifts and changes in position and changes in Full Width at Half Maximum (FWHM). The plots of  $I_D/I_G$  as a function of FWHM for the 143 single-point spectra in Raman mapping were fitted (**Figure 3i**), indicating the existence of basal plane defects rather than edge defects in the Cu-N<sub>2</sub>@HNOC since the  $I_D/I_G$  is correlated with the FWHM (G)<sup>[27]</sup>, which is consistent with the XAS fitting.

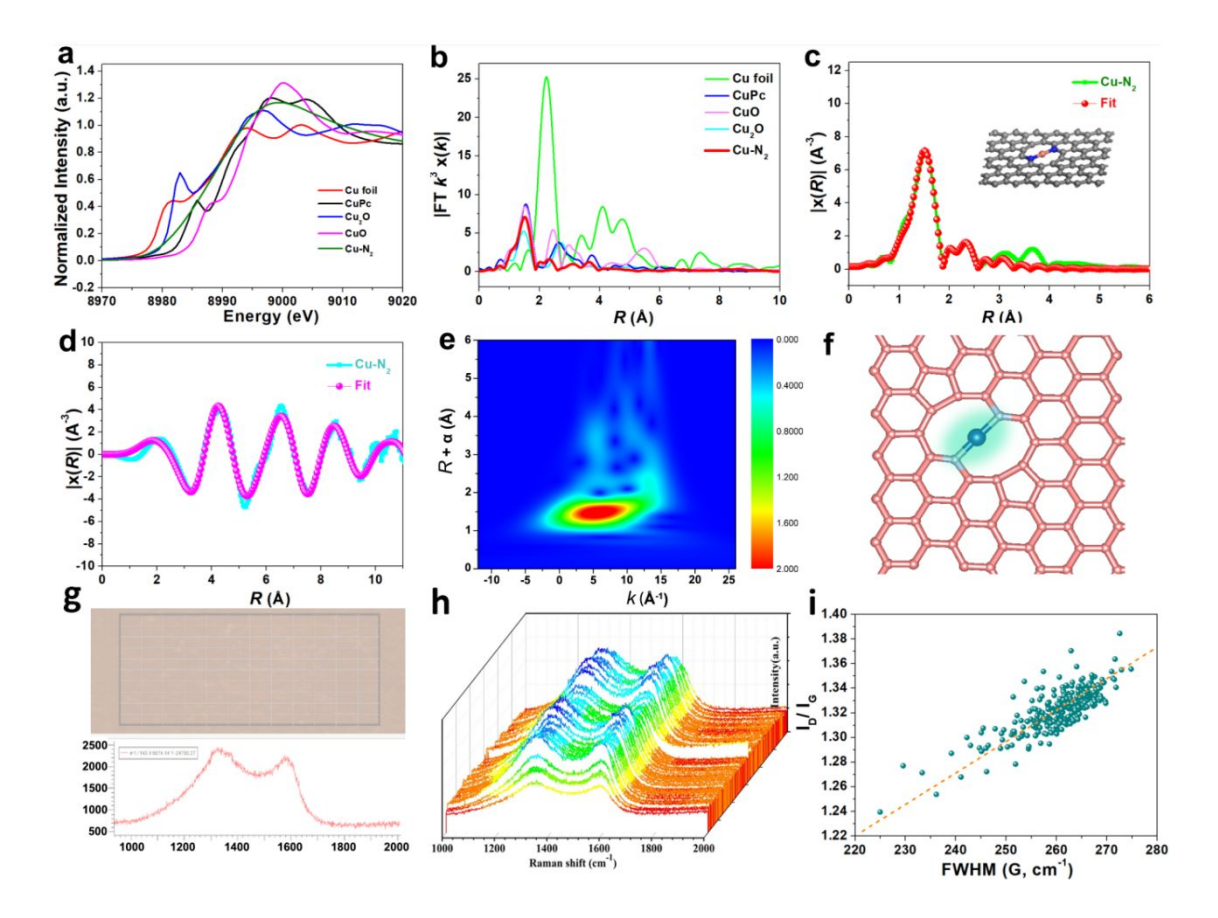


**Figure 3**. Cu k-edge XANES spectra (a) and Fourier-transformed EXAFS (b) of Cu-N<sub>2</sub>@HNOC, Cu foil, CuPc, Cu<sub>2</sub>O and CuO; The Cu EXAFS fitting curve in R space (c) and in k space (d) of Cu k-edge with Cu-N<sub>2</sub> model; (e) The corresponding WT plots; (f) Schematic model of Cu-N<sub>2</sub> structure; (g) Raman mapping image and typical Raman spectrum; (h) 143 single-point spectra in Raman mapping area; (i) The plots of  $I_D/I_G$  as a function of FWHM for the 143 single-point Raman spectra in Cu-N<sub>2</sub>@HNOC.

In addition, the porosity and specific surface area were investigated by the  $N_2$  adsorption/desorption isotherm (**Figure S15a**). The curve for Cu- $N_2$ @HNOC belongs to Type IV isotherms, indicating abundant mesopores. The pore size distribution curves (inset) displayed that the pore size is mainly distributed under 10 nm, referring to abundant micro/mesopores located on the octahedron surface. The hollow and hierarchical porous structure provides the prerequisite for highly-efficient ORR process due to accelerated electron/mass transport and more exposed active sites<sup>[28-30]</sup>. To further explore the effect of Cu- $N_2$  sites, we prepared hollow N-doped octahedron

carbon (HNOC) as control samples for comparison. The XRD and Raman techniques for HNOC and Cu-N<sub>2</sub>@HNOC were performed to get an insight into the crystal structures and defects. As shown in **Figure S15b**, all the XRD curves displayed a broadened peak located at ~26° assigned to carbon. In comparison, the peaks for Cu-N<sub>2</sub>@HNOC shift negatively compared to that for HNOC, which might be due to the incorporation of Cu atoms resulting in a larger lattice spacing. The Raman spectra in **Figure S15c** present the value of  $I_D/I_G$ . Specifically, the values of Cu-N<sub>2</sub>@HNOC (1.32) are much larger than that of HNOC (1.07), indicating the introduction of Cu atoms will lead to higher defect densities thus providing more active sites for ORR<sup>[3,31]</sup>.

The electrochemical catalytic activity toward ORR was investigated by the RDE technique in 0.1 M KOH solution. Figure 4a depicts the cyclic voltammetry (CV) on different electrodes. Obviously, all the CV curves exhibit quasi-rectangular capacitive background current in N<sub>2</sub>-saturated solution, but possess a strong oxygen reduction peak in O<sub>2</sub>-saturated solution. Moreover, the peak for Cu-N<sub>2</sub>@HNOC (0.84 V) located at the most positive position is much more positive than that for HNOC (0.70 V). It signifies that the Cu-N<sub>2</sub>@HNOC electrode possesses better catalytic activity towards ORR. This supposition is also supported by linear sweep voltammetry (LSV) results. As shown in **Figure 4b**, the Cu-N<sub>2</sub>@HNOC electrode presents prominent activity with more positive onset potential ( $E_{\text{onset}}$ , 0.93 V) and half-wave potential ( $E_{1/2}$ , 0.83 V) and a higher limiting current density  $(J_1)$  of 5.81mA/cm<sup>2</sup> compared with the Pt/C electrode  $(E_{\text{onset}} = 0.92\text{V}, E_{1/2} = 0.81\text{V}, J_{\text{I}} = 5.48 \text{ mA/cm}^2)$ . Moreover, the LSV curves at different rotation rates and the corresponding K-L plots at different potentials of Cu-N<sub>2</sub>@HNOC are given in Figure 4c. The electron transfer number (n) at the potential range from 0.2 V to 0.4 V indicated a one-step reaction mechanism following with the direct fourelectron transfer pathway. In order to discern the reaction kinetics, the kinetic current density  $(J_k)$  at the potential of 0.75 V and Tafel plot were obtained as shown in **Figure**  4d and 4e. Compared with other counterparts, the Cu-N<sub>2</sub>@HNOC electrode exhibits higher values of  $J_k$  (23.6 mA/cm<sup>2</sup>) and smaller Tafel slopes (80 mV/dec), suggesting its faster reaction kinetics and better ORR activity. The superior electrochemical performance of Cu-N<sub>2</sub>@HNOC is associated with the synergistic effect of highly active unsaturated Cu-N<sub>2</sub> sites and hollow porous structures. The resultant electronic structure furnishes prominent activity. It is well-known that metal-N structure is sensitive to SCN<sup>-</sup>, thus, we employed SCN<sup>-</sup> solution to detect the Cu-N<sub>x</sub> active site. As shown in **Figure S16**, the ORR activity of Cu-N<sub>2</sub>@HNOC exhibited a significant drop after adding 0.01 M SCN<sup>-</sup>, illustrating the blockage of Cu-N<sub>2</sub> site. Whereas, HNOC catalyst displays no significant variation because the SCN<sup>-</sup> cannot poison the nitrogen catalytic sites<sup>[13]</sup>. In addition, the durability test was conducted by chronoamperometric tests. As revealed in **Figure 4f**, the current recession of Cu-N<sub>2</sub>@HNOC is only 6.5 % after 20,000 s, but the loss for Pt/C is 18.3 %. The SEM image of Cu-N<sub>2</sub>@HNOC after ORR cycling is presented in **Figure S17**. As shown, Cu-N<sub>2</sub>@HNOC retains its original octahedral morphology without any collapse. Clear, Cu-N<sub>2</sub>@HNOC displays considerable stability, which is ascribed to the intrinsic thermodynamic structural stability of Cu-N<sub>2</sub> Lewis acid sites, as well as the hollow octahedron structure with abundant hierarchical pores avoiding the possible collapse during the mass and electron transport[13,14]. Furthermore, methanol tolerance test was also conducted (Figure S18). A sharp current loss happened to Pt/C after the introduction of 3 M methanol. In contrast, negligible degradation can be seen for Cu-N<sub>2</sub>@HNOC, suggesting superior anti-methanol poison ability.

To assess the potential for practical application, the obtained  $Cu-N_2@HNOC$  was applied as the cathode catalyst in home-made Zn-air batteries (ZABs, **Figure 4g**). The ZABs assembled with the  $Cu-N_2@HNOC$  displayed an open-circuit voltage of 1.44 V, which is higher than that of Pt/C (1.37V, **Figure 4h**). As shown in **Figure 4i**, the ZABs

based on Cu-N<sub>2</sub>@HNOC delivered a peak power density of 190 mW/cm<sup>2</sup> at a current density of 312 mA/cm<sup>2</sup>, superior to that of Pt/C (139 mW/cm<sup>2</sup> at 241 mA/cm<sup>2</sup>) under the same condition. The Cu-N<sub>2</sub>@HNOC catalyst also exhibits good rate performance as revealed in Figure 4j, since there is only a small voltage drop when the current density increases to 20 mA/cm<sup>2</sup> and the voltage can recover to the initial value once the current density returns to 1 mA/cm<sup>2</sup> Therefore, ZABs based on Cu-N<sub>2</sub>@HNOC catalyst can drive a small fan benefiting from the high power density (Figure 4k) and two ZABs can be integrated in series to power light emitting diode (LED 3 V) bulbs (**Figure 4I**). Additionally, primary ZABs with the Cu-N<sub>2</sub>@HNOC catalyst also have favorable durability and rate performance. Normalized to the mass of consumed Zn, the specific capacity of Cu-N<sub>2</sub>@HNOC was calculated to be 700.82 mAh/kg<sub>Zn</sub> (**Figure S19a**). The galvanostatic discharge curves at 5 mA/cm<sup>2</sup> (**Figure S19b**) display a stable discharge potential of 1.27 V and only slight decline of output voltage was observed within nearly 45 hours, demonstrating excellent stability. Furthermore, rechargeable ZABs were also constructed with the mixture of RuO<sub>2</sub> and Cu-N<sub>2</sub>@HNOC catalyst. It was discerned that only a very small voltage change happened after 200 cycles (**Figure S20**), suggesting an excellent rechargability and application potentials<sup>[32]</sup>.

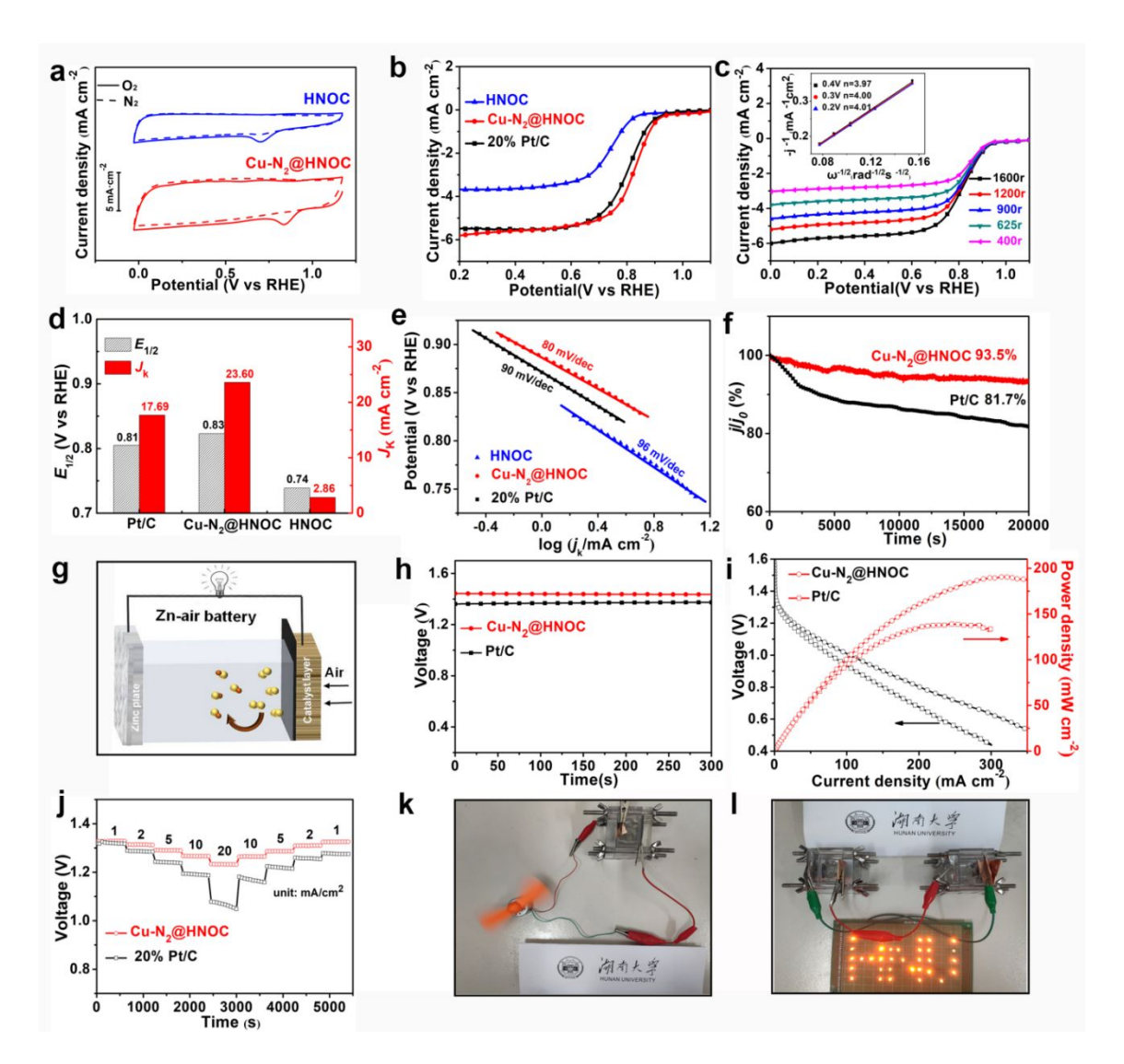


**Figure 4**. (a) CV curves in  $N_2/O_2$  saturated 0.1 M KOH electrolyte and (b) LSV curves at the rotation rate of 1600 rpm of various electrocatalysts; (c) LSV curves of Cu- $N_2$ @HNOC electrode at different rotation rates from 400 to 1600 rpm and the corresponding K-L plots (inset); Comparison of  $E_{1/2}$  and  $J_k$  values (d) and Tafel slopes (e) on different electrocatalysts; (f) Chronoamperometric curves on Cu- $N_2$ @HNOC and 20 % Pt/C catalysts; (g) Schematic illustration of aqueous ZABs assembled with Cu- $N_2$ @HNOC as cathode catalysts; (h) Open circuit voltage measurements (i) Discharge polarization curves and the power density curve; (j) Discharge curves at various current densities; (k) Photograph of a fan powered by one Zn-air battery; (l) Photograph of some red light-emitting diode (LED) bulbs powered by two Zn-air batteries connected in series.

To further prove the practical applications of Cu-N<sub>2</sub>@HNOC for the Zn-air battery devices, flexible solid-state Zn-air batteries were also fabricated. The stability and flexibility of solid state Zn-air batteries were promoted by a casting-drying polyvinyl alcohol (CD-PVA) gel electrolyte (10\*10 cm<sup>2</sup> CD-PVA film in Figure 5a). The optimized CD-PVA film possesses a maximum tensile stress of 13.5 MPa, which is ten times higher than the normal PVA film (Figure 5b). Moreover, the ion mobility of CD-PVA film is also higher than the normal one (Figure S21). A Ni foam and CD-PVA film were used as current collector and solid-state electrolyte. The optimized Zn-air battery delivers high open circuit voltage of 1.39 V (Figure 5c). Notebly, only a small voltage drop was observed in **Figure 5d** for Cu-N<sub>2</sub>@HNOC when the current density increases from 1 to 10 mA cm<sup>-2</sup>, suggesting its excellent rate performance<sup>[33, 34]</sup>. As shown in Figure 5e, Cu-N<sub>2</sub>@HNOC catalyst displays a peak power density of 78.1 mW cm<sup>-2</sup>, much higher than that of Pt/C under the same condition. The performance tests on flexible solid-state Zn-air batteries with various bending angles have also been conducted. As shown in the Figure S22, Zn-air battery delivered high open circuit voltage of 1.360, 1.387, 1.336 and 1.349 V when bended at 0°, 45°, 90° and 120°, respectively. Furthermore, when the Cu-N<sub>2</sub>@HNOC-based flexible Zn-air battery was folded in different bending states, only a negligible increase in voltage gap can be observed in Figure S23, demonstrating its exceptional mechanical robustness and operational stability<sup>[35]</sup>. In addition, Cu-N<sub>2</sub>@HNOC catalyst based Zn-air battery presents favorable durability with no obvious voltage change after cycling for a long time, suggesting a promising application prospect (Figure 5f). Besides, the Zn-air battery with Cu-N<sub>2</sub>@HNOC catalyst operates well under acid electrolyte (pH=4-5) with voltage of 1.0-1.1 V for discharging and 2.0-2.1 V for charging (Figure 5g, the first report for SSZABs under acidic condition). Furthermore, the solid-state Zn-air batteries with only ~3 cm<sup>2</sup> achieved a high power density ascribed to the high catalytic activity of Cu-N<sub>2</sub>@HNOC, which is able to light up LED series in the "HNU" shape (**Figure 5h**). In a word, the Zn-air battery with Cu-N<sub>2</sub>@HNOC cathode is still competitive with the state-of-the-art Zn-air batteries (**Figure 5i and Table S9**) up to date.

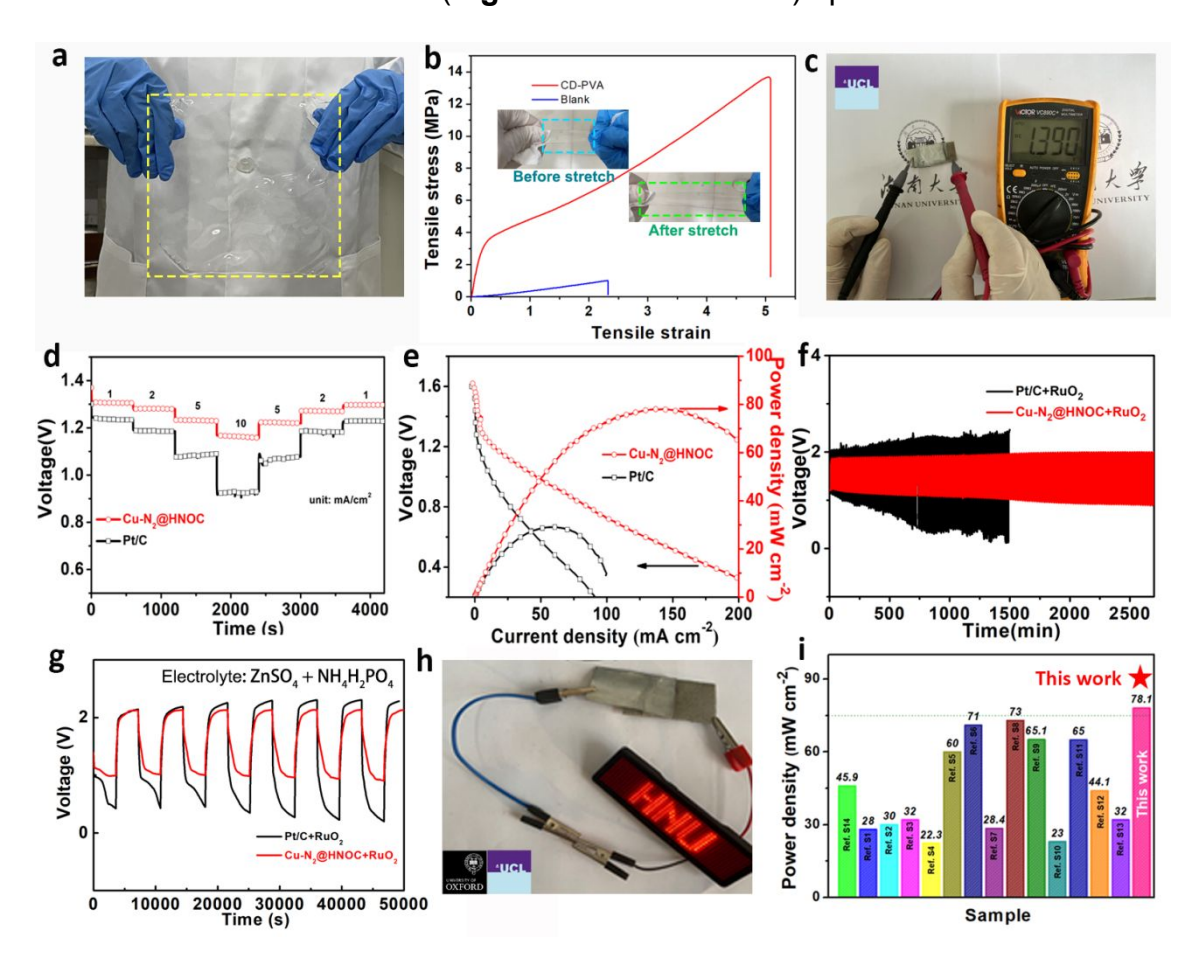


**Figure 5.** (a) Optical image of CD-PVA film; (b) the tensile stress of CD-PVA and normal PVA, inset: the optical images before and after stretch; (c) the diagram of flexible solid-state Zn-air batteries and the open voltage; (d) Rate performance, (e) Polarization and power density and (f) Galvanostatic charge-discharge at 3 mA cm<sup>-2</sup> for solid-state Zn-air batteries with different electrocatalysts; (g) The charging-discharging curve of solid-state Zn-air batteries in acid electrolyte (1 M ZnSO<sub>4</sub>+ NH<sub>4</sub>H<sub>2</sub>PO<sub>4</sub>, pH=4-5); (h) Photographs of LED light charged by solid-state Zn-air batteries; (i) The comparison of the Cu-N<sub>2</sub>@HNOC Zn-air battery with representative work reported previously.

# 4. Limitation and Perspective

One limitation of this work is the insufficiency of high-quality data. While there are numerous structures available from both theoretical and experimental perspectives, the lack of a standardized protocol renders the results incomparable, and datasets in existing studies may yield misleading outcomes. Addressing this limitation could significantly improve the research, but it may necessitate support from the entire scientific community in the future. Another bottleneck is the expressiveness of chemical structure models. Enhancing the development of more expressive architectures can feasibly be integrated into the multi-modal pretraining framework. For future directions, we aim to establish a universal platform and standardized protocol for retrieving catalyst-activity-stability relations via virtual screening (VS). These results would be continuously updated following experimental validation. With the accumulation of high-quality input datasets, accurately predicting electrocatalyst structures to achieve desired properties could be achieved more effectively.

# 5. Conclusion

In summary, a computer VS standard protocol was developed and built up by combining MD simulations, DFT calculations, and ML. A thermodynamically stable yet coordination unsaturated Cu-N<sub>2</sub> Lewis acid site was discovered to possess promising electrochemical activity via this protocol. The as-screened Cu-N<sub>2</sub> Lewis acid site was fabricated in a Cu-N<sub>2</sub>@HNOC through a facile *in-situ* polymerization followed with a pyrolyzation strategy using CuO octahedrons as self-sacrificial templates. The obtained Cu-N<sub>2</sub>@HNOC exhibits excellent performance in ORR and ZABs, which is attributed to the synergistic effect of hollow nitrogen-doped carbon structures and highly active unsaturated Cu-N<sub>2</sub> sites. Specifically, the unsaturated coordination of Cu-N<sub>2</sub> Lewis acid sites can modulate the charge distribution, adsorption energy and hydrophilicity, and thus improve catalytic activity, as predicted by the DFT calculations, MD simulations, and validated through the experimental results. The thermodynamic

and catalytic operating stability of the unsaturated linear Cu-N<sub>2</sub> site were verified by MD simulation. The thermodynamic stable yet coordination unsaturated Cu-N<sub>2</sub> Lewis acid sites provide new insights and good guidance for the search and design of high-performance Cu-based electrocatalysts. Although the current protocol is used to screen the Cu-N-C based catalysts, it could be used for discovering multiple types of functional materials.

# **Supporting Information**

Supporting Information is available and includes supplementary notes, figures (S1-S23) and tables (S1-S9).

#### **Author contributions**

Huanxin Li conceived and designed the idea and co-wrote the paper and supervised the entire project and are responsible for the infrastructure and project direction. Chenxi Xu, Kaiqi Li, Shengchao Liu, and Huanxin Li discussed the idea, wrote the code, experimentally realized the study, analysed the data and co-wrote the paper, and these works were assisted by Junwei Xu, Subash Sharma, Jincan Zhang, Boyang Mao, Haotian Chen, Hao Zhang, Hannan Xu, Bingcheng Luo, Haiteng Zhao, Zhuoxinran Li, Zhongyuan Huang, Jianan Wang, Kai Xi, Chaopeng Fu, Yunlong Zhao, Guoliang Chai, Guanjie He, and Ivan Parkin. All the authors discussed the results, commented on and revised the manuscript.

#### **Conflict of Interest**

The authors declare no conflict of interest

#### **Acknowledgements**

This work was supported by National Natural Science Foundation of China (Grant No. 52274298, 51974114, 51672075, and 2190804), International Postdoctoral Exchange Followship Program (Grant No. PC2022020), Natural Science Foundation of Hunan Province (Grant No. 2024JJ4022, 2025JJ60382), Scientific Research Fund of Hunan Provincial Education Department (Grant No. 24B0270), Technology Innovation Program of Hunan Province (2020RC2024), and China Postdoctoral Science Foundation (2020M682560, GZC20233205). National Super-computing Center (TIANHE) in CHANGSHA is acknowledged for allowing the use of computational resources. K. L. would like to thank China Scholarship Council/UCL Dean's Prize for the joint PhD funding. EPSRC is thanked for funding through EP/L015862/1. Richard G. Compton from the University of Oxford assisted with the proofreading of the manuscript.

# **Preprint Acknowledgement**

Research presented in this article was posted on a preprint server prior to publication in CCS Chemistry. The corresponding preprint article can be found here: 10.21203/rs.3.rs-3635532/v1.

### References

- [1] Gallagher, J. Oxygen reduction reaction: Counting active sites. *Nat. Energy* **2016**, *1*, 16198.
- [2] Zhou, Y.; Yu, Y.; Ma, D.; Foucher, A. C.; Xiong, L.; Zhang, J.; Stach, E. A.; Yue, Q.; Kang, Y. Atomic Fe Dispersed Hierarchical Mesoporous Fe–N–C Nanostructures for an Efficient Oxygen Reduction Reaction. *ACS Catal.* **2021**, *11*, 74–81.
- [3] Sun, Z.; Wang, Y.; Zhang, L.; Wu, H.; Jin, Y.; Li, Y.; Shi, Y.; Zhu, T.; Mao, H.; Liu, J.; Xiao, C.; Ding, S. Simultaneously Realizing Rapid Electron Transfer and Mass

- Transport in Jellyfish–Like Mott–Schottky Nanoreactors for Oxygen Reduction Reaction. *Adv. Funct. Mater.* **2020**, *30*, 1910482.
- [4] Chen, H.; Liang, X.; Liu, Y.; Ai, X.; Asefa, T.; Zou, X. Active Site Engineering in Porous Electrocatalysts. *Adv. Mater.* **2020**, *32*, 2002435.
- [5] Li, H.; Gong, Y.; Zhou, H.; Li, J.; Yang, K.; Mao, B.; Zhang, J.; Shi, Y.; Deng, J.; Mao, M.; Huang, Z.; Jiao, S.; Kuang, Y.; Zhao, Y.; Luo, S. Ampere–hour–scale soft–package potassium–ion hybrid capacitors enabling 6–minute fast–charging. *Nature Commun.* **2023**, 14, 6407.
- [6] Yang, X.; Zheng, X.; Li, H.; Luo, B.; He, Y.; Yao, Y.; Zhou, H.; Yan, Z.; Kuang, Y.; Huang, Z. Non–Noble–Metal Catalyst and Zn/Graphene Film for Low–Cost and Ultra–Long–Durability Solid–State Zn–Air Batteries in Harsh Electrolytes. *Adv. Funct. Mater.* **2022**, 32, 2200397.
- [7] Shen, H.; Gracia–Espino, E.; Ma, J.; Zang, K.; Luo, J.; Wang, L.; Gao, S.; Mamat, X.; Hu, G.; Wagberg, T.; Guo, S. Synergistic Effects between Atomically Dispersed Fe–N–C and C–S–C for the Oxygen Reduction Reaction in Acidic Media. *Angew. Chem. Int. Ed.* **2017**, *56*, 13800–13804.
- [8] Cheng, R.; He, X.; Li, K.; Ran, B.; Zhang, X.; Qin, Y.; He, G.; Li, H.; Fu, C.; Rational Design of Organic Electrocatalysts for Hydrogen and Oxygen Electrocatalytic Applications. *Adv. Mater.* **2024**, 2402184.
- [9] Wu, J.; Zhou, H.; Li, Q.; Chen, M.; Wan, J.; Zhang, N.; Xiong, L.; Li, S.; Xia, B. Y.; Feng, G.; Liu, M.; Huang, L. Densely Populated Isolated Single Co–N Site for Efficient Oxygen Electrocatalysis. *Adv. Energy Mater.* **2019**, *9*, 1900149.
- [10] Xu, C.; Wu, J.; Chen, L.; Gong, Y.; Mao, B.; Zhang, J.; Deng, J.; Mao, M.; Shi, Y.; Hou, Z.; Cao, M.; Li, H.; Zhou, H.; Huang, Z.; Kuang, Y. Boric Acid—Assisted Pyrolysis for High—Loading Single—Atom Catalysts to Boost Oxygen Reduction Reaction in Zn—Air Batteries. *Energy Environ. Mater.* **2024**, 7, e12569.

- [11] Zhao, L.; Zhang, Y.; Huang, L. B. Liu, X. Z.; Zhang, Q. H.; He, C.; Wu, Z. Y.; Zhang, L. J.; Wu, J.; Yang, W.; Gu, L.; Hu, J. S.; Wan, L.J. Cascade Anchoring Strategy for General Mass Production of High–Loading Single–Atomic Metal–Nitrogen Catalysts. *Nat. Commun.* **2019**, *10*, 1278.
- [12] Li, J.; Chen, J.; Wang, H.; Ren, Y.; Liu, K.; Tang, Y.; Shao, M. Fe/N Co-Doped Carbon Materials with Controllable Structure as Highly Efficient Electrocatalysts for Oxygen Reduction Reaction in Al-Air Batteries. *Energy Storage Mater.* **2017**, *8*, 49–58.
- [13] Huang, Z.; Pan, H.; Yang, W.; Zhou, H.; Gao, N.; Fu, C.; Li, S.; Li, H.; Kuang, Y. *In Situ* Self-Template Synthesis of Fe–N-Doped Double-Shelled Hollow Carbon Microspheres for Oxygen Reduction Reaction. *ACS Nano* **2018**, *12*, 208–216.
- [14] Tan, Z.; Li, H.; Feng, Q.; Jiang, L.; Pan, H.; Huang, Z.; Zhou, Q.; Zhou, H.; Ma, S.; Kuang, Y. One-Pot Synthesis of Fe/N/S-Doped Porous Carbon Nanotubes for Efficient Oxygen Reduction Reaction. *J. Mater. Chem. A* **2019**, *7*, 1607–1615.
- [15] Lai, Q.; Zhu, J.; Zhao, Y.; Liang, Y.; He, J.; Chen, J. MOF-Based Metal-Doping-Induced Synthesis of Hierarchical Porous Cu-N/C Oxygen Reduction Electrocatalysts for Zn–Air Batteries. *Small* **2017**, *13*, 1700740.
- [16] Zhang, Y.; Liu, J.; Wang, J.; Zhao, Y.; Luo, D.; Yu, A.; Wang, X.; Chen, Z. Engineering Oversaturated Fe-N<sub>5</sub> Multifunctional Catalytic Sites for Durable Lithium-Sulfur Batteries. *Angew. Chem. Int. Ed.* **2021**, *60*, 26622-26629.
- [17] Li, P.; Jin, Z.; Qian, Y.; Fang, Z.; Xiao, D.; Yu, G. Supramolecular Confinement of Single Cu Atoms in Hydrogel Frameworks for Oxygen Reduction Electrocatalysis with High Atom Utilization. *Mater. Today* **2020**, *35*, 78–86.
- [18] Yang, Z.; Chen, B.; Chen, W.; Qu, Y.; Zhou, F.; Zhao, C.; Xu, Q.; Zhang, Q.; Duan, X.; Wu, Y. Direct Transformation of Copper(I) Oxide Bulk into Isolated Single-Atom

Copper Sites Catalyst through Gas-Transport Approach. *Nat. Commun.* **2019**, *10*, 3734.

[19] Lai, Q.; Zheng, L.; Liang, Y.; He, J.; Zhao, J.; Chen, J. Metal–Organic-Framework-Derived Fe-N/C Electrocatalyst with Five-Coordinated Fe-N<sub>x</sub> Sites for Advanced Oxygen Reduction in Acid Media. *ACS Catal.* **2017**, *7*, 1655–1663.

[20] Li, F.; Han, G.-F.; Noh, H.-J.; Kim, S.-J.; Lu, Y.; Jeong, H. Y.; Fu, Z.; Baek, J.-B. Boosting Oxygen Reduction Catalysis with Abundant Copper Single-Atom Active Sites. *Energy Environ. Sci.* **2018**, *11*, 2263–2269.

[21] Wu, H.; Li, H.; Zhao, X.; Liu, Q.; Wang, J.; Xiao, J.; Xie, S.; Si, R.; Yang, F.; Miao, S.; Guo, X.; Wang, G.; Bao, X. Highly Doped and Exposed Cu(I)–N Active Sites within Graphene towards Efficient Oxygen Reduction for Zinc–Air Batteries. *Energy Environ. Sci.* **2016**, 9, 3736–3745.

[22] Yang, J.; Liu, W.; Xu, M.; Liu, X.; Qi, H.; Zhang, L.; Yang, X.; Niu, S.; Zhou, D.; Liu, Y.; Su, Y.; Li, J.; Tian, Z. Q.; Zhou, W.; Wang, A.; Zhang, T. Dynamic Behavior of Single-Atom Catalysts in Electrocatalysis: Identification of Cu-N<sub>3</sub> as an Active Site for the Oxygen Reduction Reaction. *J. Am. Chem. Soc.* **2021**, 143, 14530-14539.

[23] Mládek A.; Gerla V.; Zazay A.; Bradáč, O. Application of Machine Learning Methods in NPH. *Normal Pressure Hydrocephalus: Pathophysiology, Diagnosis, Treatment and Outcome. Cham: Springer International Publishing*, **2023**, 359-386.

[24] Li, J.; Xia, W.; Wang, T.; Zheng, L.; Lai, Y.; Pan, J.; Jiang, C.; Song, L.; Wang, M.; Zhang, H.; Chen, N.; Chen, G.; He, J. A Facile Route for Constructing Effective Cu-N<sub>x</sub> Active Sites for Oxygen Reduction Reaction. *Chem. Eur. J.* **2020**, *26*, 4070–4079.

[25] Jiang, Z.; Sun, W.; Shang, H.; Chen, W.; Sun, T.; Li, H.; Dong, J.; Zhou, J.; Li, Z.; Wang, Y.; Cao, R.; Sarangi, R.; Yang, Z.; Wang, D.; Zhang, J.; Li, Y. Atomic Interface Effect of a Single Atom Copper Catalyst for Enhanced Oxygen Reduction Reactions.

Energy Environ. Sci. 2019, 12, 3508-3514

[26] Liu, X.; Liu, Y.; Jin, M.; Xu, C.; Tian, Y.; Zhou, M.; Wang, W.; Li, G.; Hou, Z.; Chen, L. Construction of N-Doped Carbon Encapsulated Mn<sub>2</sub>O<sub>3</sub>/MnO Heterojunction for Enhanced Lithium Storage Performance. *J. Colloid Interface Sci.* **2024**, 665, 752–763. [27] Ferrari, A. C.; Basko, D. M.Raman Spectroscopy as a Versatile Tool for Studying the Properties of Graphene.. *Nat. Nanotechnol.* **2013**, *8*, 235–246.

[28] Liu, Y. P.; Xu, C. X.; Ren, W.Q.; Hu, L. Y.; Fu, W. B.; Wang, W.; Yin, H.; He, B. H.; Hou, Z. H.; Chen, L. Self-Template Synthesis of Peapod-Like MnO@N-Doped Hollow Carbon Nanotubes as an Advanced Anode for Lithium-Ion Batteries. *Rare Met.* **2023**, 42, 929–939.

[29] Zhou, L.; Zhuang, Z.; Zhao, H.; Lin, M.; Zhao, D.; Mai, L. Intricate Hollow Structures: Controlled Synthesis and Applications in Energy Storage and Conversion. *Adv. Mater.* **2017**, *29*, 1602914.

[30] Zhu, W.; Chen, Z.; Pan, Y.; Dai, R.; Wu, Y.; Zhuang, Z.; Wang, D.; Peng, Q.; Chen, C.; Li, Y. Functionalization of Hollow Nanomaterials for Catalytic Applications: Nanoreactor Construction. *Adv. Mater.* **2019**, *31*, 1800426.

[31] Hou, J.; Sun, Y.; Wu, Y.; Cao, S.; Sun, L. Promoting Active Sites in Core–Shell Nanowire Array as Mott–Schottky Electrocatalysts for Efficient and Stable Overall Water Splitting. *Adv. Funct. Mater.* **2018**, *28*, 1704447.

[32] Li, H.; Wen, Y.; Jiang, M.; Yao, Y.; Zhou, H.; Huang, Z.; Li, J.; Jiao, S.; Kuang, Y.; Luo, S. Understanding of Neighboring Fe-N<sub>4</sub>-C and Co-N<sub>4</sub>-C Dual Active Centers for Oxygen Reduction Reaction. *Adv. Funct. Mater.* **2021**, *31*, 2011289.

[33] Li, S.; Chen, W.; Pan, H.; Cao, Y.; Jiang, Z.; Tian, X.; Hao, X.; Maiyalagan, T.; Jiang, Z. FeCo Alloy Nanoparticles Coated by an Ultrathin N-Doped Carbon Layer and Encapsulated in Carbon Nanotubes as a Highly Efficient Bifunctional Air Electrode for Rechargeable Zn-Air Batteries. *ACS Sustainable Chem. Eng.* **2019**, 7, 8530-8541.

[34] Rao, P.; Yu, Y.; Wang, S.; Zhou, Y.; Wu, X.; Li, K.; Qi, A.; Deng, P.; Cheng, Y.; Li, J.; Miao, Z.; Tian X. Understanding the Improvement Mechanism of Plasma Etching Treatment on Oxygen Reduction Reaction Catalysts. *Exploration*. **2023**, 20230034.

[35] Hao, X.; Jiang, Z.; Zhang, B.; Tian, X.; Song, C.; Wang, L.; Maiyalagan, T.; Hao, X.; Jiang, Z. N-Doped Carbon Nanotubes Derived from Graphene Oxide with Embedment of FeCo Nanoparticles as Bifunctional Air Electrode for Rechargeable Liquid and Flexible All-Solid-State Zinc-Air Batteries. *Adv. Sci.* **2021**, 8, 2004572.

# **Table of Contents Graphic**

